IEEE Access
Multidisciplinary | Rapid Review | Open Access Journal

Received April 28, 2022, accepted May 27, 2022, date of publication May 30, 2022, date of current version June 6, 2022.

Digital Object Identifier 10.1109/ACCESS.2022.3179401

Design of Boost-Type Power Factor Correction With Stepped Air-Gap Ferrite Inductor for Peak-Power-Load Condition

JING-YUAN LIN, (Member, IEEE), PIN-HSIEN LIU, HSUAN-YU YUEH, AND YI-FENG LIN
Department of Electronic and Computer Engineer, National Taiwan University of Science and Technology, Taipei City 106335, Taiwan
Corresponding author: Jing-Yuan Lin (jylin@mail.ntust.edu.tw)

ABSTRACT This paper presents the designed method and the implementation of stepped air-gap ferrite inductor applied in power factor correction (PFC). Conventionally, the input inductor of the PFC has a designed consideration on the maximum output power; thus, designing the PFC for peak-power-load conditions results in a very large inductor. The proposed designed method improves the load-carrying capability without increasing the volume of the inductor when the PFC is operating in peak-power-load conditions. The stepped air-gap ferrite inductor maintains the inductance in the rated-full-load and sustains the peak-power-load conditions with the lower inductance. Compared with the conventional ferrite inductor, the proposed method can maintain the size and the efficiency of the power supply, and promote the power-carrying ability. The detailed analysis and the design of the proposed method are described. Experimental results are recorded and evaluated by a prototype PFC with an AC input voltage of 110–264 VAC and a DC output voltage of 384 VDC. Finally, the volume of input inductor is kept with 40950 mm^2, the efficiency is also same compared with the conventional inductor, and the load-carrying capability of the converter is promoted from the normal rated power of 1 kW to the peak power load of 2 kW.

INDEX TERMS Power factor correction, stepped air-gap inductor, peak power.

I. INTRODUCTION

In the century of green energy, the power industry is striving for high efficiency and power density of converters. Fig. 1 shows that power factor correction (PFC) has the benefits ranging from reducing the demand charges on the power system to increasing the effectiveness of power usage. It shapes the input current of the power supply to synchronize with the input voltages and avoid large harmonic current. The input current of PFC should also comply with the standard regulation [1]. Besides, the PFC converter has been applied in disk drives, motor derives, fans, and pump derivers. These applications require a large output power at the duration of start-up and are usually higher than the rated-full-load conditions. Therefore, the inductor of the PFC converter is designed for peak-power-load conditions, but the volume and the cost of the inductor are evidently increased and wasted.

In reference [2]–[5], the active technique is proposed to inject the magnetic flux to input inductor and solved the saturation of the inductor in peak-load conditions. However, this method might result in the redundant circuit and complicating the control strategy. In reference [6], [7], the configurable inductor is proposed to control the inductance and applied in wide load range converter. However, this method will additionally complex the control of the switches on inductor which might increase the switching loss and EMI problems. In reference [8], [9], the coupled inductor is introduced and used in interleaved CCM boost PFC converter. Although, the DC magnetic flux can be canceled in the coupled inductor. The interleaved architecture is only suited for high power levels. In reference [10], a small piece of permanent magnet is added in to the air gap. The permanent DC magnetic field will double the saturation current with the same size

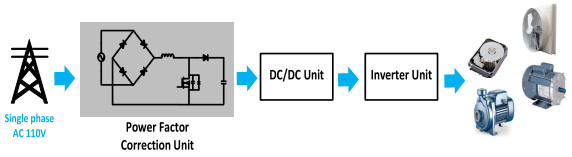

FIGURE 1. Power flow with PFC.

The associate editor coordinating the review of this manuscript and approving it for publication was Chi-Seng Lam.

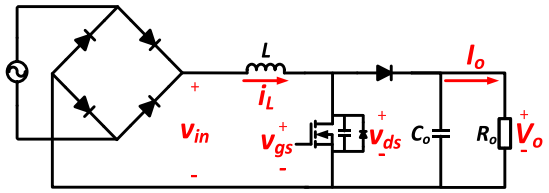

FIGURE 2. Boost-type PFC.

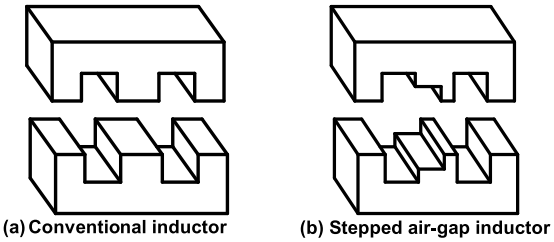

FIGURE 3. Geometry of proposed inductor and conventional inductor.

of inductor. However, this method will shape the permanent magnet into flaky shape. The reliability of the permanent magnet will be questioned. In this paper, the passive method is proposed and adopted in single phase CCM boost PFC converter. The stepped air-gap ferrite inductor can ensure high inductor current with smaller volume and be used in so many applications [11]. However, the non-linear characteristic of the stepped air-gap inductor is hard to analysis. In [12], [13], the characteristic curve of inductor is depicted with asymptote. This method is precise, but hard to quantitative analysis. In [14], [15], the B-H curve of the ferrite is decomposition into linear subproblem. This helps the mathematic module to approximate the real characteristic of the stepped air-gap inductor, easily. Even so, [14], [15] still lack of an intuitive method to find out the boundary inductor current. In this paper, the stepped air-gap ferrite inductor is analyzed according to the magnetoresistance to help realize the composition of the equation and applied in the boost-type PFC converter. The proposed geometry shape of ferrite inductor is utilized to reduce the volume and sustain more current through the duration of peak-power-load conditions. The boost input inductor is not saturated. Thus, input current total harmonic distortion (iTHD) can be maintained for the standard regulation [16], [17]. Compared with the conventional geometry shape of the ferrite inductor, the proposed inductor can also maintain the same conversion efficiency of the converter at normal-rated-power conditions with smaller volume. According to the above, the calculated modules of the stepped air-gap inductor are introduced in section II, and the simulated results are also verified. Besides, the designed progress of the stepped air-gap ferrite inductor is presented in section III. Finally, theoretical discussions are validated with the experimental results on a prototype PFC circuit that delivers an AC input of 110–264 V_{AC} and a DC output of 385 V_{DC} with convectional inductor and stepped air-gap inductor, respectively.

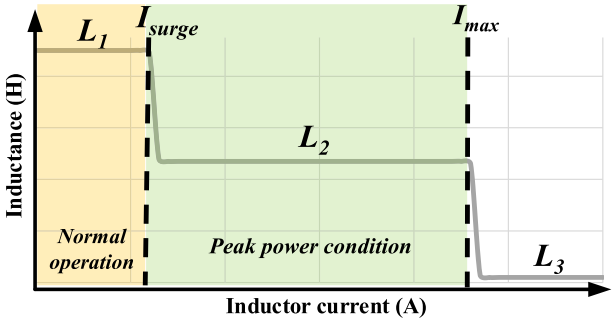

FIGURE 4. Proposed stepped air-gap inductor.

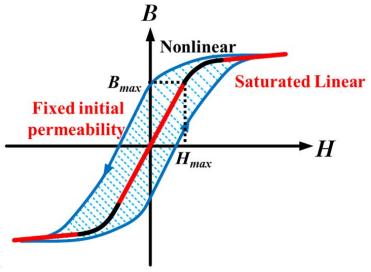

FIGURE 5. Nonlinear B-H curve of ferrite material.

II. PROPOSED METHOD

The boost type PFC converter is shown Fig. 2. From the average current method, the greater output power enhances the inductor current and pushes the magnetic flux of the conventional inductor to the limit. Thus, the input inductor might become fully saturated and cause a large short-circuit current in peak-power operation. To solve this problem, a stepped air-gap inductor is proposed, as shown in Fig. 3. The equivalent inductance under different load currents is designed, as shown in Fig. 4. When the PFC converter is operated in normal conditions, the inductance is a constant value L_1, which is designed to achieve the requirement of current ripple. When the PFC converter is operated in peak-power conditions, inductance drops to L_2 and enters the second state to provide a higher load-carrying ability. Equation (1) depicts the phase angle θ of the input current when inductance drops.

$$\theta = sin^{-1}\left(\frac{V_{in\_rms} \cdot I_{surge}}{\sqrt{2} \cdot P_o}\right) \tag{1}$$

To calculate the inductance varying with the operating current, the following assumptions are introduced. First, core loss is neglected. The magnetization of the material, especially soft ferrite, makes the magnetic component shift the domain boundaries (Bloch wall) [18] over imperfections in the crystallite. Hence, the irreversible movement causes hysteresis loss [19], [20] and varies initial permeability, as shown in Fig. 5. Under this assumption, the B-H curve can be modeled into three sections, namely, fixed initial permeability, nonlinear, and saturated linear.

When the operating current is below I_{surge}, the inductor is operated in L_1 region, and the ferrite core is not saturated deeply. In Fig. 6, Ansys Maxwell shows that the magnetic

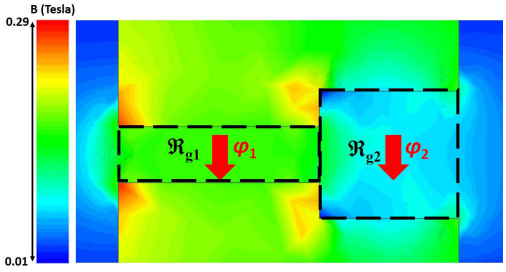

FIGURE 6. Magnetic flux density of stepped air-gap inductor with inductor current below I_{surge}.

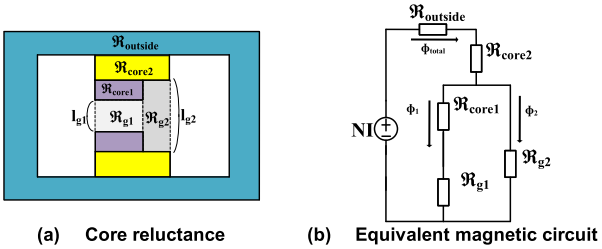

FIGURE 7. Reluctance of stepped air-gapped inductor.

flux, φ_1 and φ_2, flows are parallel in the proposed inductor. Thus, the equivalent magnetic circuit can be shown in Fig. 7, and L_1 can be expressed in Equation (2) by Faraday's law. The magnetic flux densities of $\Re_{core1}$ and $\Re_{core2}$ are expressed in Equations (3) and (4), respectively. Where N represents the turns number of the inductor. A_{e_min} and A_e respectively represent the effective cross-section area of $\Re_{core1}$ and $\Re_{core2}$.

$$L_1 = \frac{N^2}{\mathcal{R}_{outside} + \mathcal{R}_{core2} + \left[\mathcal{R}_{g2} // \left(\mathcal{R}_{core1} + \mathcal{R}_{g1}\right)\right]} \approx \frac{N^2}{\mathcal{R}_{g1} // \mathcal{R}_{g2}} \tag{2}$$

$$B_1(I) = \frac{L_1}{A_{e\_min}} \cdot \frac{I}{N} \cdot \frac{\mathcal{R}_{g2}}{\mathcal{R}_{g1} + \mathcal{R}_{g2}} \tag{3}$$

$$B_2(I) = \frac{L_1}{A_e} \cdot \frac{I}{N} \tag{4}$$

where

$$R_{g1} = \frac{l_{g1}}{\mu_0 \cdot A_{e\_min}} \tag{5}$$

$$R_{g2} = \frac{l_{g2}}{\mu_0 \cdot \left(A_e - A_{e\_min}\right)} \tag{6}$$

When the operating current of the inductor is over I_{surge}, the $\Re_{core1}$ of the stepped air-gap inductor operates in the nonlinear section and is saturated gradually. The inductance rolls off rapidly until $\Re_{core1}$ is saturated deeply as Ansys Maxwell simulation shows in Fig. 8. Hence, the equivalent magnetic circuit can be predicted as a model in Fig. 9. The inductance L_2 and the magnetic flux density of $\Re_{core2}$ can be expressed in Equations (7) and (8), respectively. I_{surge} can be

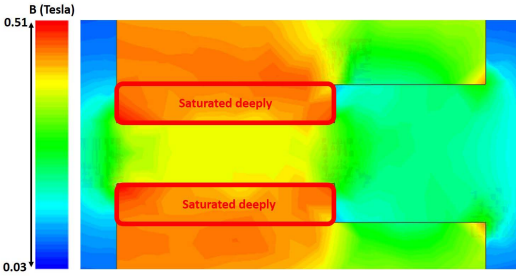

FIGURE 8. Magnetic flux density of stepped air-gap inductor with inductor current between I_{surge} and I_{max}.

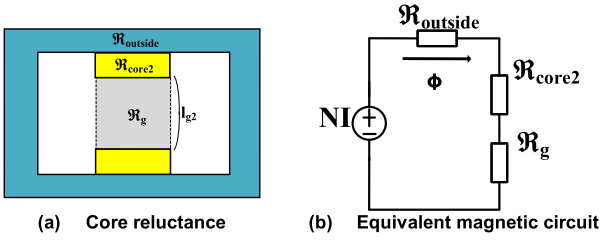

FIGURE 9. Reluctance of stepped air-gapped inductor.

also expressed in Equation (9).

$$L_2 = \frac{N^2}{\mathcal{R}_{outside} + \mathcal{R}_{core2} + \mathcal{R}_g} \approx \frac{N^2}{\mathcal{R}_g} \tag{7}$$

$$B_2(I) = \frac{L_2}{A_e} \cdot \frac{I}{N} \tag{8}$$

$$I_{surge} = \frac{N \cdot B_{max} \cdot A_{e\_min}}{L_1} \cdot \frac{\mathcal{R}_{g1} + \mathcal{R}_{g2}}{\mathcal{R}_{g2}} \tag{9}$$

where

$$R_g = \frac{l_{g2}}{\mu_0 \cdot A_e} \tag{10}$$

When the operating current is over I_{max}, $\Re_{core2}$ and $\Re_{outside}$ are deeply saturated, and the inductance falls rapidly to L_3 region. Therefore, this condition causes a large short-circuit current through the power switch of the PFC converter, and the design of the stepped air-gapped inductor should avoid this situation region. I_{max} can be expressed as Equation (11).

$$I_{max} = \frac{N \cdot B_{max} \cdot A_e}{L_2} \tag{11}$$

III. DESIGNED PROGRESS OF PEAK POWER APPLICATION

In the peak-power-load application places, the conventional design the air-gap inductor uses a bulky inductor for peak-power load because the large input current causes the inductor to become deeply saturated [21]–[23]. In this section, the design method of the stepped air-gap inductor is presented to solve the above problems. Fig. 10 shows the designed flow of the stepped air-gap inductor. First, the specification of the PFC circuit including the inductance of the inductor in regular-load conditions, the volume, and the material of the inductor should be confirmed. Table 1 shows the comparison

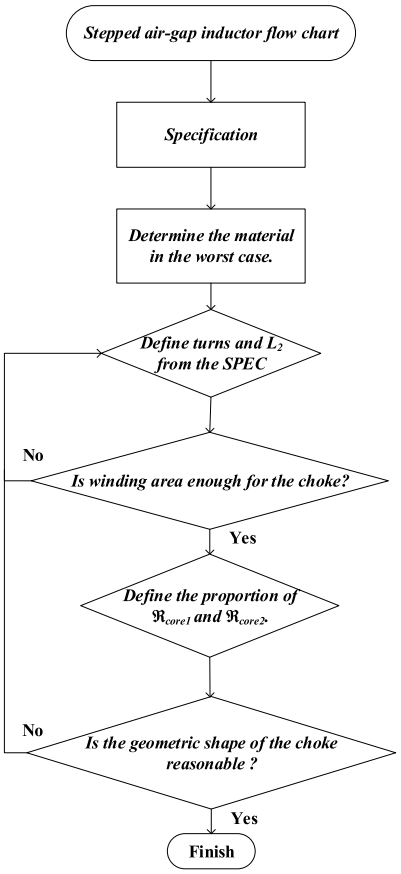

FIGURE 10. Designed progress of stepped air-gap inductor.

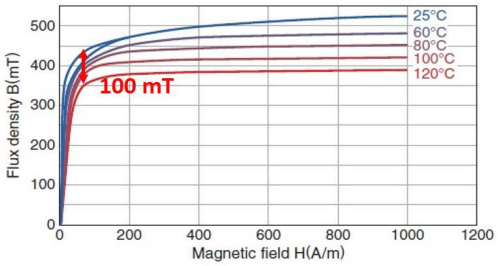

FIGURE 11. B-H curve of soft material of PC47.

between soft and hard magnetic material of the inductor. Soft ferrites, such as 3C96 and PC47 of TDK corporation [24], are recommended for the application of the stepped air-gap inductor. Compared with the powder core [25], the soft ferrite has not only lower core loss and copper loss but also cheaper. In addition, ferrite core has a drastic variation on permeability according to DC magnetizing force. These advantages help in designing the stepped air-gap inductor. The environment temperature in the worst case should also be considered. Fig. 11 shows the influence of environment temperature on PC47. The saturated magnetic flux density has a 100 m Tesla difference between 25 °C and 120 °C.

Second, to achieve the volume requirement of the peak-load operation, (11) can help designers optimize L_2 wisely.

TABLE 1. Comparison of magnetic material.

Parameter	Ferrite core (Soft)	Powder core (Hard)
Space utilization	high	low
Saturation Flux Density (B_{sat})	low	high
Core loss	low	high
Copper loss	low	high
Price	low	high

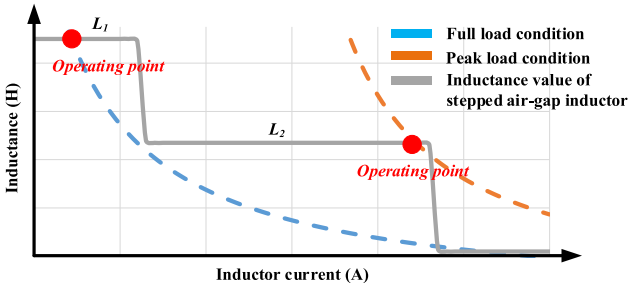

FIGURE 12. Stepped air-gap inductor curve and IL_max curve at full-load and peak-load conditions.

Moreover, inductance L_1 can be optimized by the concern of current ripple and efficiency in normal operation (I_L below I_{surge}). Finally, the designers can determine the proper proportion of $\Re_{core1}$ and $\Re_{core2}$ by using (9).

In the application of PFC converter, the maximum inductor current I_{L_max}, varies with input inductance and output power. With average current method, the relationship can be easily found out and expressed as Equation (12). Additionally, the designers can overlay (12) with Fig. 4 as Fig.12 shown. Thus, the designed inductor can be sure to operate in L_1 region in full load conditions and operate in L_2 region in peak load conditions.

$$L\left(I_{L\_max}, P_o\right) = \frac{\sqrt{2}\cdot V_{in\_rms}\cdot\left(1-\frac{\sqrt{2}\cdot V_{in\_rms}}{V_o}\right)}{2\cdot f_s\left(I_{L\_max}-\frac{\sqrt{2}\cdot P_o}{V_{in\_rms}}\right)} \quad (12)$$

IV. EXPERIMENTAL RESULTS

To confirm the validity of the proposed method, the normal power 1 kW prototype of the PFC converter is implemented and promoted to 2 kW with stepped air-gap inductor. The specification of the prototype is shown in TABLE 2. Besides, the components are also listed in TABLE 2. They are chosen based on the peak inductor current. Inductance, 110 and 55 μH, are selected as L_1 and L_2 of stepped air-gap inductor in full-load and peak-load conditions, respectively. Finally, the inductor is presented in Fig. 13. The proposed inductor can handle peak power operation. TABLE 3 shows that the volume of the inductor is also limited as the conventional one. However, the turns are increased to 36 turns to widen the load range of operation further.

The stepped air-gap inductor is compared with the conventional air-gap inductor in the case of same turns and volume. Based on finite element simulation software, fringing

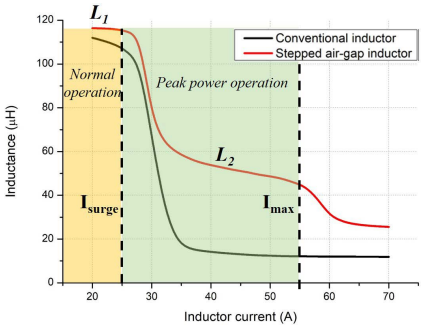

FIGURE 13. Inductance measurement results.

TABLE 2. Specification and resonant parameters.

Parameter	Value
Input voltage	110~264 VAC
Output voltage	384 V
Normal rated maximum power	1 kW
Peak power	2 kW
Operating frequency	65 kHz
Bridge rectifier	GBJ50006
Main switches	STW70N65M2
Diode	CVFD20065A

TABLE 3. Designed parameters of inductor.

Parameter	Conventional inductor	Stepped air-gap inductor
Inductance, L_1	110 μH	110 μH
Inductance, L_2		55 μH
I_{surge}	25 A	25 A
I_{max}		55 A
Volume	40950 mm^2	40950 mm^2
A_e	266 mm^2	266 mm^2
B_{max}	320 mT	320 mT
Turns	30	36

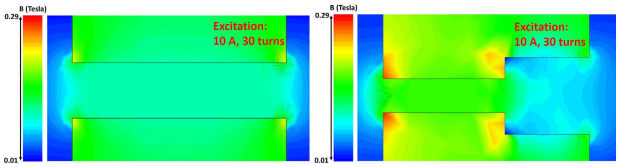

FIGURE 14. The magnetic flux density of the two inductors.

loss, core loss, and copper loss are included. Moreover, the same DC triangle current excites both inductors, as shown in Fig. 14. The loss simulation results are shown in Table 4. The benefits of the proposed inductor can raise not only the performance of the magnetic component but also the load-carrying capability. In TABLE 4, the proposed inductor has smaller fringing-flux effect on winding and improves the total copper loss of the inductor. The core loss is also reduced because of the difference of the geometry between two inductors.

In the AC analysis, since the behavior of the average quantities has great effect in converters. The influence of the stepped change on inductor can be verified by the three-terminal PWM switch model proposed in [26]. Accord-

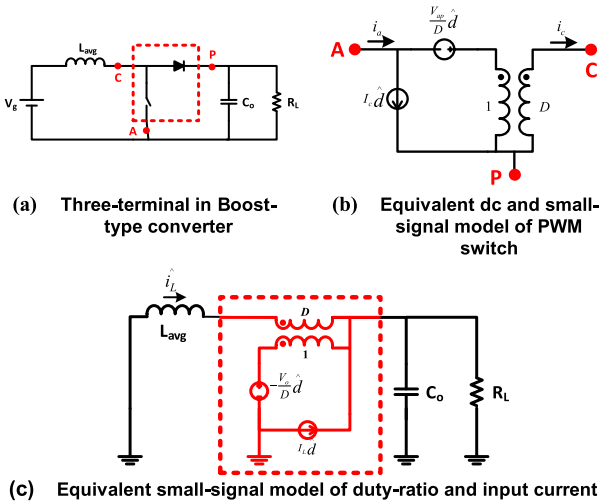

FIGURE 15. Small signal model of PWM switch.

TABLE 4. Loss comparison between the two inductors.

Parameter	Conventional inductor	Stepped air-gap inductor
Core Loss	0.14 W	0.11 W
Copper Loss	21.6 W	20.3 W
Total Loss	21.7 W	20.4 W

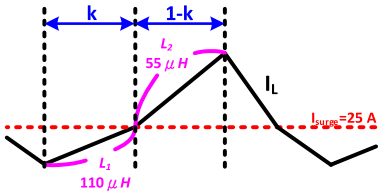

FIGURE 16. The time proportion of inductor current.

ing to three-terminal PWM switch model in Fig. 15(a), the equivalent dc and small-signal model of PWM switch is shown as Fig. 15(b). The voltage source and the current source depend on the terminal voltage and current in Equation (13) and (14). Where D represents the duty-ratio, and $\hat{d}$ represents the small signal of the duty-ratio. In this model, the value of stepped air-gap inductor is based on the inductor current. Thus, the average quality of the inductor, L_{avg}, can be modeled as Equation (15) and shown in Fig. 15(c). Where k is the time proportion constant of inductor current depicted in Fig. 16.

$$\hat{i_a} = D\hat{i_c} + I_c\hat{d} \tag{13}$$

$$\hat{v_{ap}} = \frac{\hat{v_{cp}}}{D} - \frac{V_{ap}}{D}\hat{d} \tag{14}$$

$$L_{avg} = \frac{1}{\frac{k}{L_1} + \frac{1-k}{L_2}} \tag{15}$$

Fig. 17 shows the dual loop control of converter. Where F_m is the modulator gain of PWM generator, R_s is the current

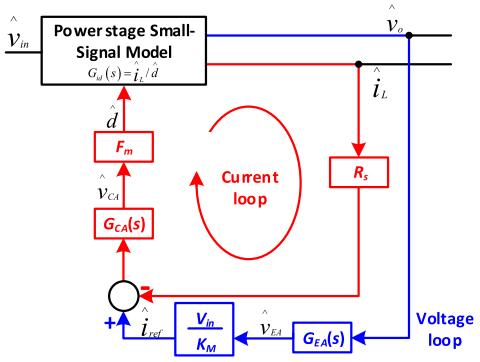

FIGURE 17. The dual loop control of the converter.

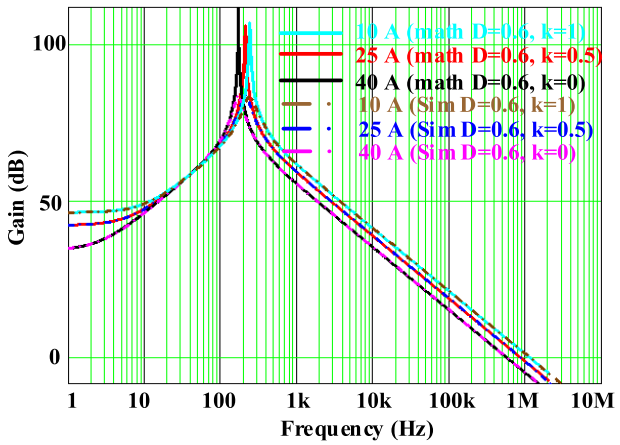

FIGURE 18. Bode plot of G_{id}.

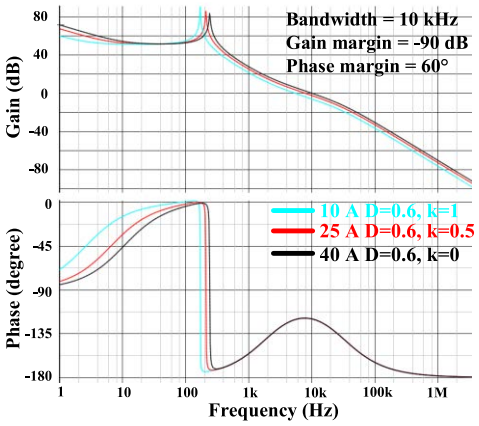

FIGURE 19. Bode plot of current loop after compensation.

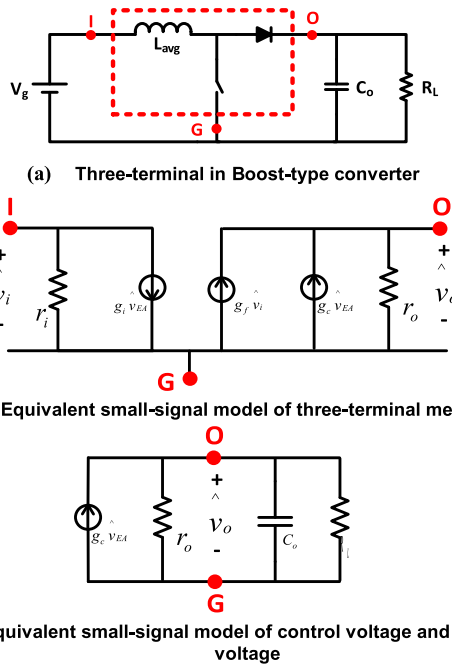

FIGURE 20. Equivalent small-signal model of G_{vc}.

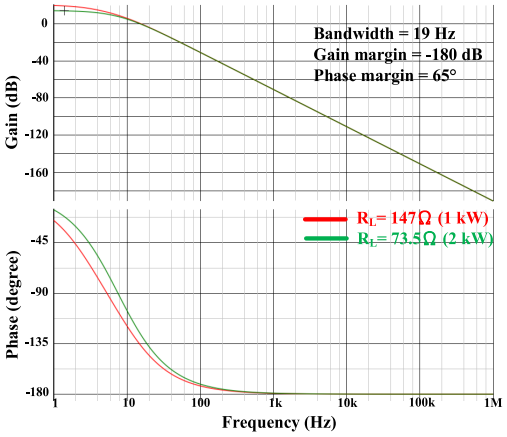

FIGURE 21. Bode plot of voltage loop after compensation.

sensed resistor, K_M is the divided voltage sensed from input line voltage. They all list in TABLE 5. Besides, G_{CA} and G_{EA} are the compensator of current loop and voltage loop, respectively. They are both 2p-2z filter in the Equation (16) and list in TABLE 6, finally. The expected duty-to-input transfer function can be thus model as Equation (17). The inductor characteristic will be changed according to different inductor current conditions and time proportion constant, k. Therefore, Fig. 18 shows the bode plot of G_{id} when the input inductor current is equal to 10A, 25A and 40A, respectively. The simulation results verified the mathematic model. Besides, the variation of the inductor doesn't affect dynamic behavior badly. The crossover frequency is just double, compared 40A with 10A. Thus, the bandwidth of the current loop can be still controlled to one-sixth of the switching frequency as Fig. 19 shown. Finally, with the compensator, G_{CA}, the bandwidth of current loop is 10 kHz, the gain margin is −90 dB, and the phase margin is 60 degree. The high-frequency current ripple of the inductor will be filtered out, successfully.

$$H(z) = \frac{B_0 + B_1 z^{-1} + B_2 z^{-2}}{A_0 + A_1 z^{-1} + A_2 z^{-2}} \tag{16}$$

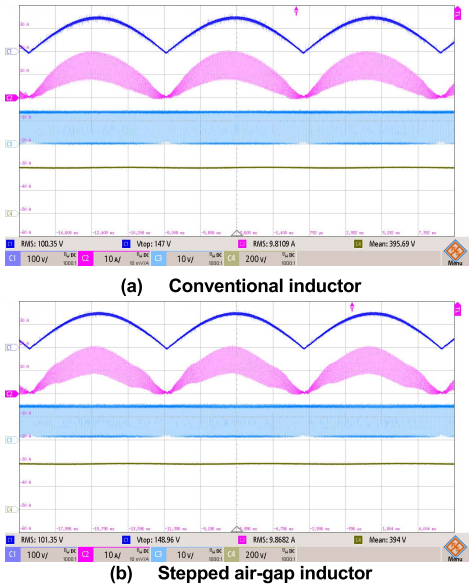

(a) Conventional inductor

(b) Stepped air-gap inductor

FIGURE 22. Key waveform of conventional inductor with 110 VAC input and 1 kW output conditions [ch1 = v_{in}, ch2 = i_L, ch3 = v_{gs}, and ch4 = V_o (Time: 2.2 ms/div)].

$$G_{id}(s) = \frac{\hat{i}_L}{\hat{d}} = K_{id}\frac{1 + s/\omega_{ZC}}{1 + s/Q\omega_o + s^2/\omega_o^2} \tag{17}$$

where

$$K_{id} = \frac{2V_o}{R_L(1-D)^2}, \quad \omega_{ZC} = \frac{2}{R_L C_o}$$
$$\omega_o = \frac{1-D}{\sqrt{L_{avg}C_o}}, \quad Q = R_L(1-D)\sqrt{C_o/L_{avg}} \tag{18}$$

For the voltage loop, to achieve stable output voltage, the bandwidth will be set to one-sixth of line-voltage frequency. The tracked input voltage will be thus view as a DC source, V_{in_rms}. In Fig. 20(a), according to the three-terminal method proposed in [27]. The ac model shown in Fig. 20(b) can be construct to illustrate the relationship between the small signals. The current source and the resistance are based on the power conversation of the input and output terminals and depicted in Equation (19). Finally, the equivalent model can be further simplified to Fig. 20(c) to discuss the influence from the command, v_{ea}, to the output voltage, v_o. The expected control-to-output transfer function can be thus model as Equation (20). It can be seen that the stepped air-gap inductor has no influence on voltage loop because of low-bandwidth. At last, with the compensator, G_{EA}, the bode plot of the voltage loop on 1 kW and 2 kW are shown in Fig. 21. The bandwidth is 19Hz, the gain margin is −180 dB, and the phase margin is 65 degree. The output voltage will be regulated at fixed voltage.

$$M = \frac{V_o}{V_{in\_rms}}, \quad r_i = \frac{r_o}{M^2}, \quad g_i = \frac{V_{in\_rms}}{K_M},$$
$$r_o = R_L g_f = \frac{2M}{r_o}, \quad g_c = \frac{V_{in\_rms}}{K_M \cdot M} \tag{19}$$

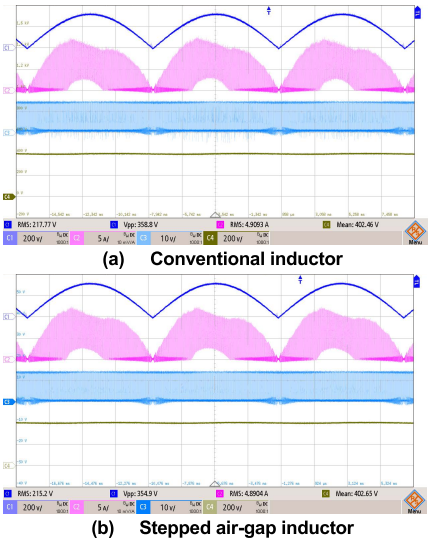

(a) Conventional inductor

(b) Stepped air-gap inductor

FIGURE 23. Key waveform of conventional inductor with 230 VAC input and 1 kW output conditions [ch1 = v_{in}, ch2 = i_L, ch3 = v_{gs}, and ch4 = V_o (Time: 2.2 ms/div)].

TABLE 5. The coefficient of the compensator.

Parameter	*Value*
F_m	0.2
R_s	1.667×10^{-4}
K_m	56.73

TABLE 6. The coefficient of the compensator.

Parameter	$G_{CA}(s)$	$G_{EA}(s)$
A_0	1	1
A_1	-0.816	-1
A_2	-0.184	0
B_0	1.779	1.014×10^{-8}
B_1	0.314	1.014×10^{-8}
$B2$	-1.465	0

TABLE 7. Comparison between the two inductors.

Parameter	Conventional inductor	Stepped air-gap inductor
Core size	40950 mm^2	40950 mm^2
Highest efficiency	93.5%	94%
Power level	1 kW	2 kW

$$G_{vc}(s) = \frac{\hat{v}_o}{\hat{v}_{ea}} = g_c \cdot \frac{r_o // R_L}{1 + sC_o(r_o // R_L)} \tag{20}$$

The experiment waveforms of conventional and stepped air-gap inductor in the full-load condition are respectively shown in Fig. 22 and 23. Both inductors are not saturated, and the waveform of both inductor current i_L are identical. Therefore, the efficiency and power factor (PF) values are similar, as shown in Fig. 24(a) and (b). The proposed inductor has the slightly lower inductance when the input voltage is 110 Vac. Thus, the RMS value of input current will be increased and slightly aggravate the conduction loss.

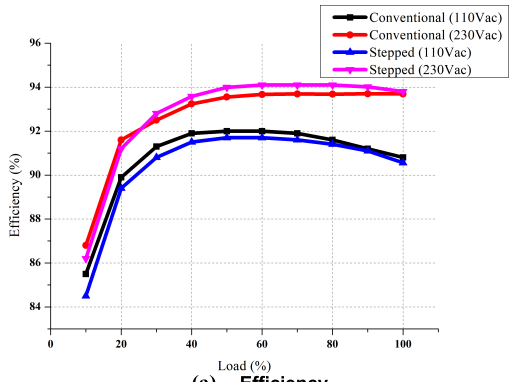

(a) Efficiency

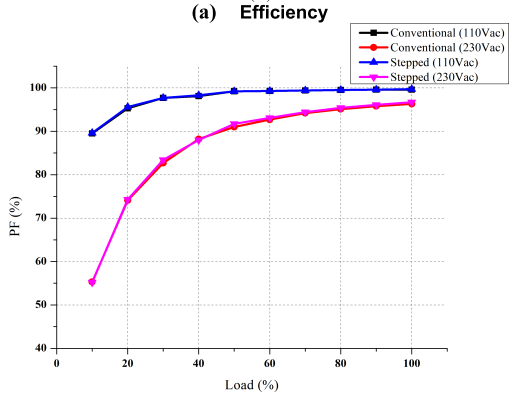

(b) PF value

FIGURE 24. Comparison between conventional and stepped air-gap inductor.

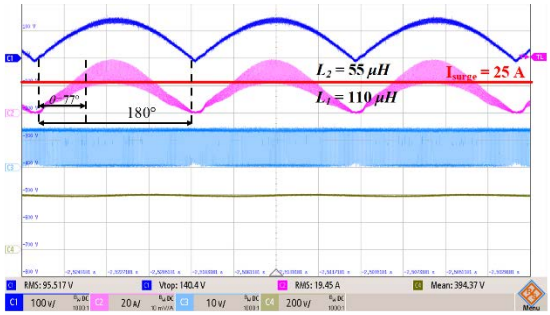

FIGURE 25. Waveform of stepped air-gap inductor with 110 VAC input and 2 kW peak power conditions [ch1 = v_{in}, ch2 = i_L, ch3 = v_{gs}, and ch4 = V_o (Time: 2.2 ms/div)].

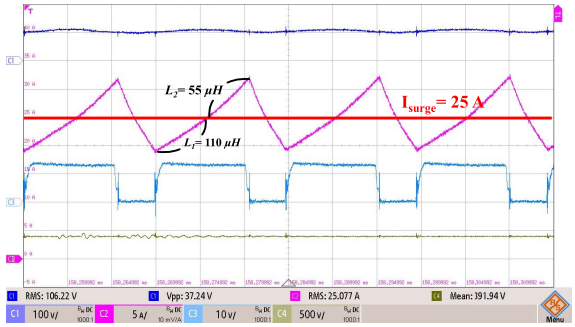

FIGURE 26. Stepped air-gap inductor variation with 110 VAC input and 2 kW peak power conditions at input current phase equal to 77° [ch1 = vin, ch2 = iL, ch3 = vgs, and ch4 = Vo (Time: 4 μs/div)].

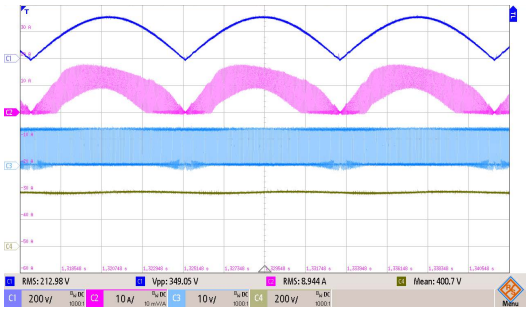

FIGURE 27. Waveform of stepped air-gap inductor with 230 VAC input and 2 kW peak power conditions [ch1 = vin, ch2 = iL, ch3 = vgs, and ch4 = Vo (Time: 2.2 ms/div)].

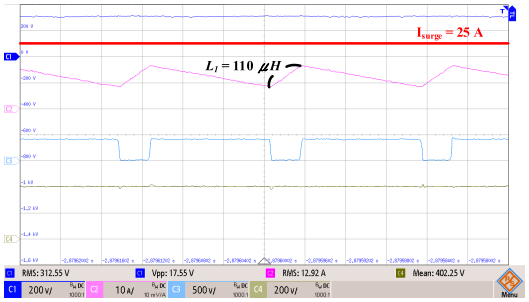

FIGURE 28. Stepped air-gap inductor variation with 230 VAC input and 2 kW peak power conditions at input current phase equal to 90° [ch1 = vin, ch2 = iL, ch3 = vds, and ch4 = Vo (Time: 4 μs/div)].

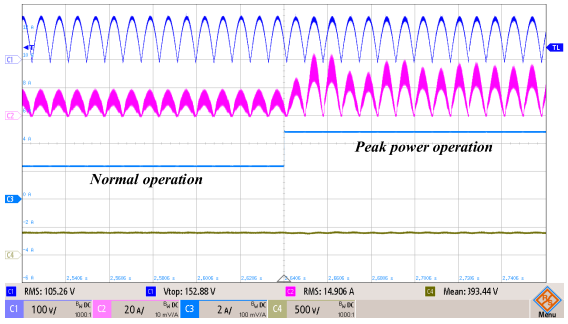

FIGURE 29. Load transient from normal-full-load conditions to peak-power-load conditions with stepped air-gap inductor (110 VAC input) [ch1 = vin, ch2 = iL, ch3 = Io, and ch4 = Vo (Time:20 ms/div)].

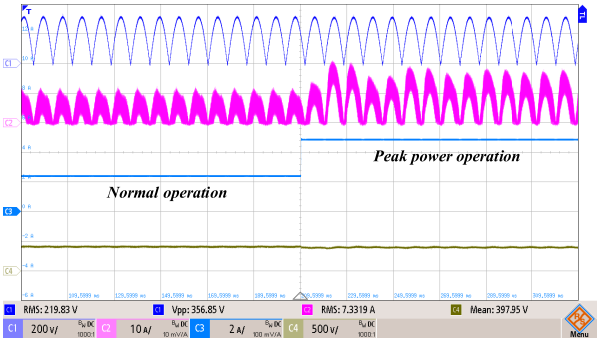

FIGURE 30. Load transient from normal-full-load conditions to peak-power-load conditions with stepped air-gap inductor (230 VAC input) [ch1 = vin, ch2 = iL, ch3 = Io, and ch4 = Vo (Time:20 ms/div)].

Fig. 25 and 26 show the key waveform of stepped air-gap inductor operated in peak-load conditions and low input voltage. The stepped air-gap inductor is reduced after 25 A, and according to (1), it occurs at the θ about 77°. Thus, the ripple of the inductor increases. Fig. 27 and 28 show the key waveform of stepped air-gap inductor operated in

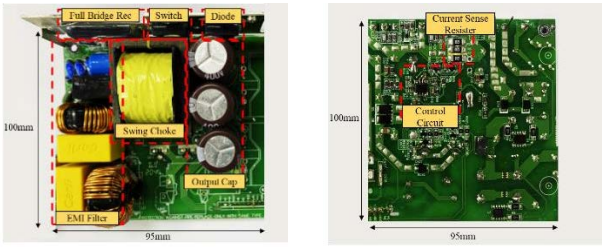

(a) Top view (b) Bottom view

FIGURE 31. Prototype of the proposed steeped air-gap inductor for PFC converter.

peak-load conditions and high input voltage. The input inductor is kept with 110 μH because the inductor current is below 25 A. Fig. 29 and 30 show the step transient responses from 1 kW to 2 kW. The converter can be regulated successfully because the variation of inductor hardly affects the dual loop control of the converter. Finally, TABLE 7 concludes the comparisons and advantages of the proposed inductor. The proposed inductor not only has the same efficiency performance but also maintain the volume of the conventional inductor. Furthermore, it promotes the power capability from 1 kW to 2 kW.

V. CONCLUSION

This paper presents a modified input inductor for the peak power application of the PFC converter. The geometry of the inductor is analyzed, and the design is presented. The stepped air-gap inductor can increase the power-carrying capability by the partial saturation of the magnetic core. Compared with the conventional inductor, the volume of the magnetic component can be effectively reduced. Moreover, the conversion efficiency and the PF value are identical with those of the conventional inductor under normal-load conditions. The validity of this paper is confirmed by the experimental results. Finally, the proposed design is fulfilled with input of 110/264 V_{AC} and output of 384 V_{DC}. The power-carrying capability of the PFC input inductor is promoted from 1 kW to 2 kW for peak-power-load conditions and the prototype is shown in Fig. 31.

REFERENCES

[1] *Electromagnetic Compatibility (EMC)—Part 3–2: Limits—Limits for Harmonic Current Emissions (Equipment Input Current ≤16 a Per Phase)*, Standard EN IEC 61000-3-2:2019, iTeh Standards Store, 2019. Accessed: Dec. 3, 2021. [Online]. Available: https://standards.iteh.ai/catalog/standards/clc/30f58587-d2d6-4393-83e1-3465764992ac/en-iec-61000-3-2-2019

[2] M. W. Beraki, J. Pedro F. Trovão, M. S. Perdigão, and M. R. Dubois, "Variable inductor based bidirectional DC–DC converter for electric vehicles," *IEEE Trans. Veh. Technol.*, vol. 66, no. 10, pp. 8764–8772, Oct. 2017.

[3] K. I. Hwu, C. W. Hsiao, and J.-J. Shieh, "Inductor saturation detection with anti-saturation control strategy applied," in *Proc. IEEE 10th Int. Conf. Power Electron. Drive Syst. (PEDS)*, Apr. 2013, pp. 266–270, doi: 10.1109/PEDS.2013.6527026.

[4] D. Medini and S. Ben-Yaakov, "A current-controlled variable-inductor for high frequency resonant power circuits," in *Proc. IEEE Appl. Power Electron. Conf. Expo. (ASPEC)*, vol. 1, Feb. 1994, pp. 219–225, doi: 10.1109/APEC.1994.316396.

[5] S. M. Ahsanuzzaman, T. McRae, M. M. Peretz, and A. Prodic, "Low-volume buck converter with adaptive inductor core biasing," in *Proc. 27th Annu. IEEE Appl. Power Electron. Conf. Expo. (APEC)*, Feb. 2012, pp. 335–339, doi: 10.1109/APEC.2012.6165840.

[6] D. Maksimovic and R. Erickson, "Universal-input, high-power-factor, boost doubler rectifiers," in *Proc. IEEE Appl. Power Electron. Conf. Expo. (APEC)*, Mar. 1995, pp. 459–465, doi: 10.1109/APEC.1995.468988.

[7] N. D. Benavides and P. L. Chapman, "Boost converter with a reconfigurable inductor," in *Proc. IEEE Power Electron. Spec. Conf.*, Jun. 2007, pp. 1695–1700, doi: 10.1109/PESC.2007.4342253.

[8] Y. Itoh, F. Hattori, S. Kimura, J. Imaoka, and M. Yamamoto, "Design method considering magnetic saturation issue of coupled inductor in interleaved CCM boost PFC converter," in *Proc. IEEE Energy Convers. Congr. Expo. (ECCE)*, Sep. 2015, pp. 2616–2621, doi: 10.1109/ECCE.2015.7310027.

[9] Q. Huang, Q. Ma, R. Yu, T. Chen, A. Q. Huang, and Z. Liu, "Improved analysis, design and control for interleaved dual-phase ZVS GaN-based totem-pole PFC rectifier with coupled inductor," in *Proc. IEEE Appl. Power Electron. Conf. Expo. (APEC)*, Mar. 2018, pp. 2077–2083, doi: 10.1109/APEC.2018.8341303.

[10] Z. Dang and J. A. Abu Qahouq, "Evaluation of high-current toroid power inductor with NdFeB magnet for DC–DC power converters," *IEEE Trans. Ind. Electron.*, vol. 62, no. 11, pp. 6868–6876, Nov. 2015, doi: 10.1109/TIE.2015.2436361.

[11] J. Kaiser and T. Durbaum, "An overview of saturable inductors: Applications to power supplies," *IEEE Trans. Power Electron.*, vol. 36, no. 9, pp. 10766–10775, Sep. 2021, doi: 10.1109/TPEL.2021.3063411.

[12] K. Stoyka, G. Di Capua, and N. Femia, "Modeling of stepped air-gap ferrite inductors in switching power supplies," in *Proc. 25th IEEE Int. Conf. Electron., Circuits Syst. (ICECS)*, Dec. 2018, pp. 401–404, doi: 10.1109/ICECS.2018.8618028.

[13] G. Di Capua and N. Femia, "A novel method to predict the real operation of ferrite inductors with moderate saturation in switching power supply applications," *IEEE Trans. Power Electron.*, vol. 31, no. 3, pp. 2456–2464, Mar. 2016, doi: 10.1109/TPEL.2015.2438952.

[14] E. Stenglein and M. Albach, "Analytical calculation method for the non-linear characteristic of ferrite-cored inductors with stepped air gap," *Electr. Eng.*, vol. 99, no. 1, pp. 421–429, Mar. 2017, doi: 10.1007/s00202-016-0432-z.

[15] E. Stenglein, D. Kuebrich, and M. Albach, "Prediction of the non-linear behavior of a stepped air gap inductor," in *Proc. IEEE 17th Workshop Control Modeling Power Electron. (COMPEL)*, Jun. 2016, pp. 1–6, doi: 10.1109/COMPEL.2016.7556674.

[16] W. Wolfle, W. G. Hurley, and S. Arnold, "Power factor correction for AC-DC converters with cost effective inductive filtering," in *Proc. IEEE 31st Annu. Power Electron. Spec. Conf.*, vol. 1, Jun. 2000, pp. 332–337, doi: 10.1109/PESC.2000.878872.

[17] W. H. Wolfle and W. G. Hurley, "Quasi-active power factor correction with a variable inductive filter: Theory, design and practice," *IEEE Trans. Power Electron.*, vol. 18, no. 1, pp. 248–255, Jan. 2003, doi: 10.1109/TPEL.2002.807135.

[18] P. Wilson, "Passive component," in *The Circuit Designer's Companion*, 4th ed. London, U.K.: Newnes, 2018.

[19] M. K. Kazimierczuk, *High-Frequency Magnetic Components*. Hoboken, NJ, USA: Wiley, 2014.

[20] S. Hasan, S. Taib, S. Hardi, A. Rahim A. R, and A. Shukri, "Core loss characteristics analysis of power transformer under different frequencies excitation," in *Proc. IEEE 7th Int. Power Eng. Optim. Conf. (PEOCO)*, Jun. 2013, pp. 619–623, doi: 10.1109/PEOCO.2013.6564622.

[21] M. Gotfryd, "Output voltage and power limits in boost power factor corrector operating in discontinuous inductor current mode," *IEEE Trans. Power Electron.*, vol. 15, no. 1, pp. 51–57, Jan. 2000, doi: 10.1109/63.817362.PFC.case.

[22] J.-S. Lai and D. Chen, "Design consideration for power factor correction boost converter operating at the boundary of continuous conduction mode and discontinuous conduction mode," in *Proc. 8th Annu. Appl. Power Electron. Conf. Expo.*, 1993, pp. 267–273, doi: 10.1109/APEC.1993.290621.

[23] D.-S. Chen and J.-S. Lai, "A study of power correction boost converter operating at CCM-DCM mode," in *Proc. Southeastcon*, 1993, p. 6, doi: 10.1109/SECON.1993.465717.

[24] *Mn-Zn Ferrite—TDK Product Center*. Accessed: Dec. 3, 2021. [Online]. Available: https://product.tdk.com/en/system/files?file=dam/doc/product/ferrite/ferrite/ferrite-core/catalog/ferrite_mn-zn_material_characteristics_en.pdf

[25] B.-G. You, B.-K. Lee, and D.-H. Kim, "Inductor design method of DCM interleaved PFC circuit for 6.6-kW on-board charger," *J. Elect. Eng. Technol.*, vol. 12, no. 6, pp. 2247–2255, 2017.
[26] V. Vorperian, "Simplified analysis of PWM converters using model of PWM switch. Continuous conduction mode," *IEEE Trans. Aerosp. Electron. Syst.*, vol. 26, no. 3, pp. 490–496, May 1990, doi: 10.1109/7.106126.
[27] R. B. Ridley, "Average small-signal analysis of the boost power factor correction circuit," in *Proc. VPEC Seminar*, 1989, pp. 108–120.

JING-YUAN LIN (Member, IEEE) was born in Kao-Hsiung, Taiwan. He received the M.S. and Ph.D. degrees in electronic engineering from the National Taiwan University of Science and Technology, Taipei, Taiwan, in 2002 and 2007, respectively. Since 2014, he has been a Faculty Member of the Department of Electronic, National Taiwan University of Science and Technology, and he is currently an Associate Professor. His research interests include the design and analysis of zero-voltage-switching DC/DC converter, power factor correction, inverter techniques, converter modeling, and power IC design.

PIN-HSIEN LIU was born in Changhua, Taiwan. He received the B.S. degree in electronic engineering from the National Taiwan University of Science and Technology, Taipei, Taiwan, in 2016, where he is currently pursuing the Ph.D. degree. His current research interests include design and analysis of the inverter control and wireless power transfer (WPT) design.

HSUAN-YU YUEH was born in Taipei, Taiwan. He received the M.S. degree in electronic engineering from the National Taiwan University of Science and Technology, Taipei, where he is currently pursuing the Ph.D. degree. His research interests include the design and analysis of the zero-voltage-switching DC/DC converters.

YI-FENG LIN was born in Yilan, Taiwan. He received the Ph.D. degree in electronic engineering from the National Taiwan University of Science and Technology, Taipei, Taiwan, in 2019. Since 2020, he has been working as a Postdoctoral Researcher with the National Taiwan University of Science and Technology. His research interests include the design and analysis of DC/DC converter, power factor correction, and DC/AC inverter.